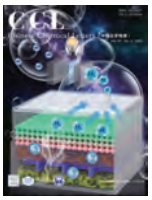
Chinese Chemical Letters 37 (2026) 111654

Contents lists available at ScienceDirect

Chinese Chemical Letters

journal homepage: www.elsevier.com/locate/cclet



Flexible gas sensors based on *in situ* fabricated hierarchically porous SnO_2/PEDOT:PSS sensing layer

Yidan Chen[a], Luyang Liu[a], Jichun Li[a], Yu Deng[a], Hongxiu Yu[a,*], Kaiping Yuan[b,*], Yuanyuan Zhang[c], Yu Wang[c,*], Yonghui Deng[a,*]

[a] *Department of Chemistry, Shanghai Stomatological Hospital & School of Stomatology, State Key Laboratory of Coatings for Advanced Equipment, Shanghai Key Laboratory of Molecular Catalysis and Innovative Materials, Fudan University, Shanghai 200433, China*
[b] *Frontier Institute of Chip and System, State Key Laboratory of Integrated Chips and Systems, Fudan University, Shanghai 200433, China*
[c] *Department of Cardiology, Shidong Hospital, Shanghai 200438, China*

ARTICLE INFO

Article history:
Received 3 June 2025
Revised 17 July 2025
Accepted 30 July 2025
Available online 30 July 2025

Keywords:
Porous materials
Organic-inorganic nanocomposites
Flexible gas sensor
PEDOT:PSS
Tin oxides
Ammonia sensor

ABSTRACT

Flexible gas sensors show promise in wearable health monitoring and toxic gas detection due to mechanical flexibility and system integration, but they still face challenges such as slow response/recovery dynamics and poor stability. Here, a novel aqueous ink consisting of n-type mesoporous tin oxide ($mSnO_2$) colloids and p-type poly(3,4-ethylenedioxythiophene)/poly(styrenesulfonate) (abbreviated as PEDOT:PSS) was designed and deposited on oxygen plasma treated polyimine (PI) substrate with pre-printed electrodes and heater *via* automatic dispension printing followed with a subsequent freeze-drying treatment, resuling in hierarchically porous sensing layer with mesopore channels and macroporous framework on the flexible PI substrate. The resultant SnO_2/PEDOT:PSS sensor showed excellent sensing performance (6 %-30.5 %) toward low-concentration ammonia (1–100 ppm), rapid response/recovery speed (61 s/25 s) and superior mechanical stability. Furthermore, the sensor was integrated into a Bluetooth-enabled smart bracelet, achieving real-time monitoring of environmetal ammonia concentration and showcasing its potential for wearable electronics in dectecting volatile harmful gases.

© 2026 Published by Elsevier B.V. on behalf of Chinese Chemical Society and Institute of Materia Medica, Chinese Academy of Medical Sciences.

The rapid advancement of emerging applications, particularly smart factories [1], smart agriculture [2], health-monitoring [3] and internet-of-things (IoTs) [4] has driven significant progress in sensor technology [5]. Chemiresistive gas sensors based on metal oxide semiconductor as the transducer have been extensively investigated and become core electronic devices owing to their ease of integration, simple preparation, and cost-effectiveness [6–9]. Among them, metal oxide semiconductors (MOS) have become the most mature and extensively studied gas sensitive materials in this field due to their high sensitivity and strong reversibility [10–12]. However, with the recent development of wearable electronics, flexible gas sensors based on polymer substrates have emerged as a leading research frontier [13,14]. These devices impose higher demands on gas sensitive materials, such as low-temperature operation and strong adhesion to flexible substrates, which limits the applicability of conventional powder MOS materials [15–17].

Conductive polymers, such as poly(3,4-ethylenedioxythiophene) /poly(styrenesulfonate) (abbreviated as PEDOT:PSS), as a branch of chemiresistive sensing materials can operate at low temperature [18], and they can be deposited by printing [19] and show strong adhesion to modified substrates like silicon, glass and plastics [20], which is favorable for fabrication of flexible gas sensors [21–24]. However, the gas sensors based on PEDOT:PSS film as the sensitive component usually suffer from limited response and slow recovery dynamics, due to their low resistance and the gas diffusion limitation imposed by the dense film structure [25–27]. To overcome the limitations, considerable efforts have been made to explore nanocomposites of PEDOT:PSS and MOS materials featuring unique morphologies and favorable heterojunctions [28,29]. In this strategy, the PEDOT:PSS serves as the main sensing component to lower operating temperature, while the heterostructure formed with inorganic MOS helps optimize the initial resistance of the sensing materials and achieve a synergical performance of powder MOS materials and conductive polymers [30,31]. Despite the progress, current research on PEDOT:PSS-based sensor still faces challenges, including the formation of a dense sensing layer after drop-casting and drying, which limits the exposure of active sites

* Corresponding authors.
E-mail addresses: hongxiuyu@fudan.edu.cn (H. Yu), kpyuan@fudan.edu.cn (K. Yuan), wangyushidonghos@163.com (Y. Wang), yhdeng@fudan.edu.cn (Y. Deng).

https://doi.org/10.1016/j.cclet.2025.111654
1001-8417/© 2026 Published by Elsevier B.V. on behalf of Chinese Chemical Society and Institute of Materia Medica, Chinese Academy of Medical Sciences.

to target gases, therefore, the porous structure sensing layer need to be design. Moreover, conventional flexbile gas sensors suffer the drawbacks of slow recovery dynamics which can be solved by intergragting an in-built heating unit for efficient desorption of gases [32,33].

Herein, through combing dispensing printing and *in situ* freeze-drying strategy, a novel colloidal ink solution consisting of mesoporous SnO_2 colloids and aqueous PEDOT:PSS solution was conveniently applied to form porous hybrid sensing layer on a fully printed, flexible, and heatable gas sensor where the heating layer and sensing electrodes were cuniningly designed to be printed on opposite sides of a polyimide (PI) substrate, enabling the sensing devices can be operated at target temperature. As a result, due to its porous morphology and significant p-n heterojunction between PEDOT:PSS and mesoporous SnO_2 which has the high specific surface area, the sensing material exhibits excellent performance in NH_3 sensing. The sensor based on the SnO_2/PEDOT:PSS material exhibited an intense response (30.5 %) to 100 ppm NH_3 at 53 °C, rapid response/recovery speed (61 s/25 s) and stable performance under mechenical deformaton. Moreover, we integrated the sensor into a smart wristband equipped with Bluetooth wireless transmission, enabling real-time signal monitoring, demonstrating its promising potential for use in smart wearable electronics. Its stable heating performance, simple fabrication process, and excellent mechanical flexibility make it a promising candidate for practical applications.

The flexible gas sensor consists of a flexible PI substrate with pre-printed Ag-heater electrodes, Ag-interdigitated electrodes (IDEs), and the hybrid sensing layer, and the design and preparation of the sensors was accomplished *via* a multi-layer printing method using the commercial printing machine (Fig. 1a). First, according to previous report with some modification [34], the colloidal mesoporous SnO_2 was prepared *via* hydrolysis of sodium stannate in the deionized water, followed by calcination in air. The field emission scanning electron microscopy (FESEM) and transmission electron microscopy (TEM) observation shows that the obtained SnO_2 nanospheres feature a uniform morphology and an ultra-small particle size of 55 nm (Fig. 1c). The high-resolution TEM (HRTEM) image (Fig. 1d) demonstrates the crystallographic

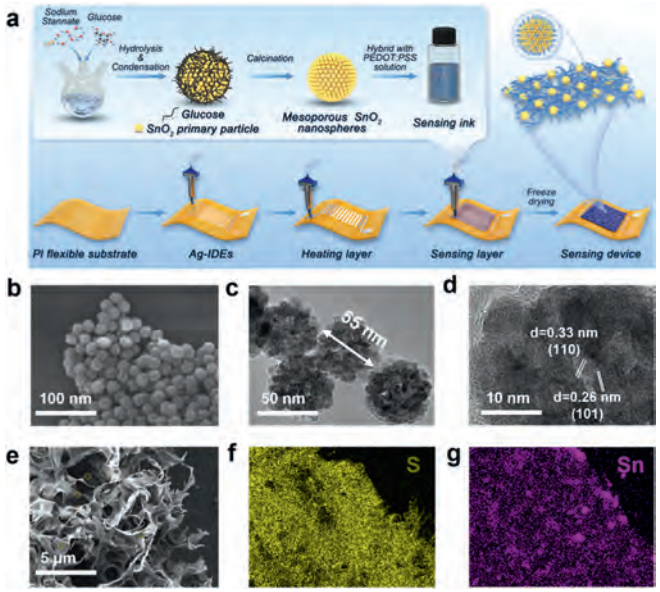


Fig. 1. (a) Preparation of the fully printed flexible gas sensing device. (b) FESEM image, (c) TEM image, and (d) HRTEM image of mesoporous SnO_2 nanospheres. (e) FESEM image of the PmS5 sensing layer on PI substrate. EDS SEM micrographs of PmS5 showing (f) S and (g) Sn elements.

planes of (110) and (101) of the cubic phase SnO_2 with corresponding lattice spacings of 0.33 and 0.26 nm, respectively. Elemental analysis by energy-dispersive X-ray spectroscopy (EDS) (Fig. S1 in Supporting information) confirmed that Sn, O are homogeneously distributed throughout the single nanosphere. X-ray diffraction (XRD) measurements confirmed the crystal structure of SnO_2 nanospheres (Fig. S2 in Supporting information). All characteristic peaks of SnO_2, corresponding to PDF #41–1445, can be clearly observed without any additional phases. N_2 adsorption-desorption measurements (Fig. S3 in Supporting information) show that the SnO_2 nanospheres possess type IV adsorption-desorption isotherms with a small hysteresis loop. The specific surface area and pore size were calculated to be 84.3 m^2/g and 2.9 nm, indicative of a high porosity of the materials.

By virtue of the hydrophilic surface property of the obtained mesoporous SnO_2 nanospheres, stable colloidal solutions can be prepared by blending mesoporous SnO_2 nanospheres and PEDOT:PSS in aqueous solutions *via* ultrasonication, and a series of homogeneous *n* wt% mesoporous SnO_2/PEDOT:PSS sensing inks (denoted as PmSn, $n = 0$, 2, 5, 9) can be prepared. The obtained colloidal ink can remain stable in 12 h when the SnO_2 content is below 9.0 wt%, while too high SnO_2 content led to partial precipitation of SnO_2 in the dispersion (Fig. S4 in Supporting information). Zeta potential measurement (Fig. S5 in Supporting information) indicates that the PmS2 and PmS5 dispersion have a zeta potential value of −65 and −71 mV, both much more negative than that (−50.0 mV) of the aqueous dispersion of mesoporous SnO_2 nanospheres, implying a good dispersion stability due to electrostatic repulsion between the nanospheres with absorbed PEDOT:PSS. Different flexible gas sensors were thus fabricated with PmS0, PmS2, and PmS5 sensing inks. Taking the PmS5-based sensor as an example, FESEM image (Fig. 1e) indicates the as-formed sensing layer after freeze-drying have numerous macropore of micrometer. By constrast, the conventional direct drying PmS5 sensing ink on PI substrate leads to continuous but dense film (Fig. S6 in Supporting information). Obviously, the macroporous structure prepared *via* the freeze-drying method can enhance the exposure of the sensing layer to the facilitating the interactions between the analyte and surface active sites. Energy dispersive spectroscopy (EDS) elemental mapping for the PmS5 layer reveals the homogeneous distribution of S and Sn elements (Figs. 1f and g), verfying the distribution of SnO_2 nanospheres in the matrix of PEDOT:PSS.

N_2 adsorption-desorption measurement (Fig. 2a) reveals that the PmS5 composite materials have a specific surface area of 32.4 m^2/g, and the pore size distribution profile shows the presence of both mesopores and macropores (Fig. 2a, inset). The lower specific surface area of PmS5 composites compared to mesporous SnO_2 demonstrates the enhanced the interface interaction betweeen the pore wall of SnO_2 and organic components during freeze-drying. In this composite, the extended polymer chains of PEDOT:PSS penetrate into the pore of mesoporous SnO_2, forming extensive heterojunctions around the SnO_2. Moreover, TEM image (Fig. S7 in Supporting information) shows that, after mixing with the hydrophilic polymers in aqueous solutons, the mesoporous SnO_2 nanospheres have a mean diameter of about 67 nm, larger than pure mesoporous SnO_2 nanospheres (Fig. 1c). HRTEM observation (Fig. S8 in Supporting information) indicates that their surface has a uniform layer (6.0 nm in thickness) of PEDOT:PSS, further comfirming the formation of the well-defined mesoporous SnO_2/PEDOT:PSS nanocomposite in PmS5.

Raman spectroscopy characterization (Fig. 2b) provides addtional evidence for the formation of mesoporous SnO_2/PEDOT:PSS nanocomposites. Compared with the Raman spectra of pure PEDOT:PSS [35], four characteristic peaks of SnO_2 were observed at 139, 468, 525, and 700 cm^{-1}. XPS analysis (Fig. 2c) shows the existence of O, Sn, C, and S. The fitted peak in the S 2p spectrum of the

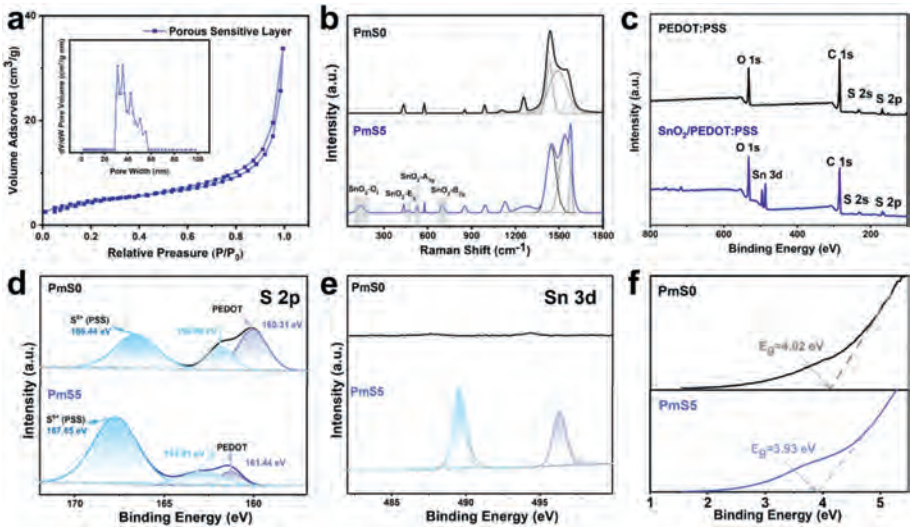


Fig. 2. (a) N_2 adsorption-desorption isotherms and pore size distribution curves (inset). (b) Raman spectra of PmS0 and PmS5. (c-e) X-ray photoelectron spectroscopy (XPS) full spectra and XPS spectra of S 2p and Sn 3d (f) Tauc plots of PmS0 and PmS5 taken form UV–vis spectra.

PmS5 composite shifts towards higher binding energy compared to PEDOT:PSS (Fig. 2d), indicating that electrons transfer from PEDOT:PSS to mesoporous SnO_2. The Sn 3d spectrum (Fig. 2e) exhibits two distinct peaks at 495.5 and 486.9 eV, corresponding to Sn $3d_{3/2}$ and Sn $3d_{5/2}$, respectively, which are the characteristics of SnO_2 [36,37]. The badgap of the PmS5 was estimated to be 3.39 eV *via* the Tauc plots from the UV–vis spectroscopy (Fig. 2f), lower than that of PmS0 (4.02 eV), indicating that PEDOT:PSS donate electrons into the conduction band of SnO_2.

In order to achieve a fully printed flexible gas sensors, Ag interdigitated electrodes (Ag-IDEs) with 9 fingers, each 6 mm in length, were printed on the flexible PI substrates (Fig. S9a in Supporting information). The FESEM (Fig. S10 in Supporting information) and optical microscopy (Fig. S9b in Supporting information) observations confirm that the electrodes exhibit a relatively uniform and well-defined structure, with a measured line width of 295 μm and line spacing of 452 μm. In addition to producing Ag-IDEs and gas sensitive layer on the frontside of the PI substrate, the heating component was printed with snake-shaped pattern on the backside of the flexible PI substrate (Fig. S11a in Supporting information), which was then encapsulated by a PI layer with thickness of 500 μm (Fig. S12 in Supporting information). Optical microscopy measurements (Fig. S11b in Supporting information) confirmed the uniform geometry of the electrodes, with a line width of 274 μm and a line spacing of 544 μm. This fabrication producrue helps make efficient use of the PI substrate space but also reduce electromagnetic interference with the interdigitated electrodes. When a voltage is applied, Joule heating is generated to provide apropriate working temperature for the gas-sensing materials. The design was further validated using COMSOL modeling and thermal field simulations, which demonstrated a highly uniform temperature distribution across the sensing materials (Fig. 3a and Fig. S13 in Supporting information). These results confirm the reliability and efficiency of the snake-shaped heating unit in the backside of PI substrate in achieving consistent thermal performance.

The stability is a critical factor in assessing the reliability of a sensor in practical applications. The heating and sensing functionalities of the flexible device were systematically tested to ensure the reliability and consistency performance over repeated cycles. Firstly, the heating performance under varying voltage was examined by measuring the tempeature of the sensing region levels using an infrared thermal camera (Fig. 3b). It indicates that the relationship between temperature and voltage aligns closely with the

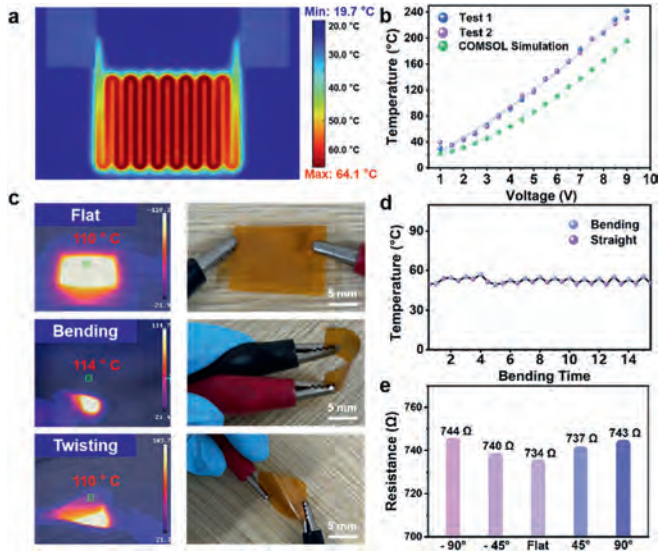


Fig. 3. (a) Thermal simulation of the heater under 4 V heating by COMSOL. (b) The relationship between the temperature of the heater and the applied voltage in the range of 1-9 V. (c) Flexibility test by measuring the temperature of the heater using the infrared thermal camera. (d) Fifteen bending tests on the heating device. (e) the initial resistance of PmS5-based sensor under different angles of bending.

trends obtained by COMSOL simulations. Additionally, the repeating measurements (Fig. 3b, Test 1 and 2) show the two overlapping curves, implying an excellent device repeatability and reliability with respect to the heat generation performance of the devices. There are two main reasons for such stable heating performance of the heating performance. On the one hand, the silver paste has the excellent electronic transfer ability and thermal stability. Within the operating temperature range, the resistance of the pre-printed electrodes remains almost unchanged; On the other hand, the encapsulation layer on the surface of the heating layer plays an important role in preventing the silver electrode from being oxidized by oxygen in the air under heating conditions and causing resistance changes.

To investigate the mechanical stability of the flexible devices, an infrared thermal camera was employed to monitor the heating performance when the PI-based devices were under different de-

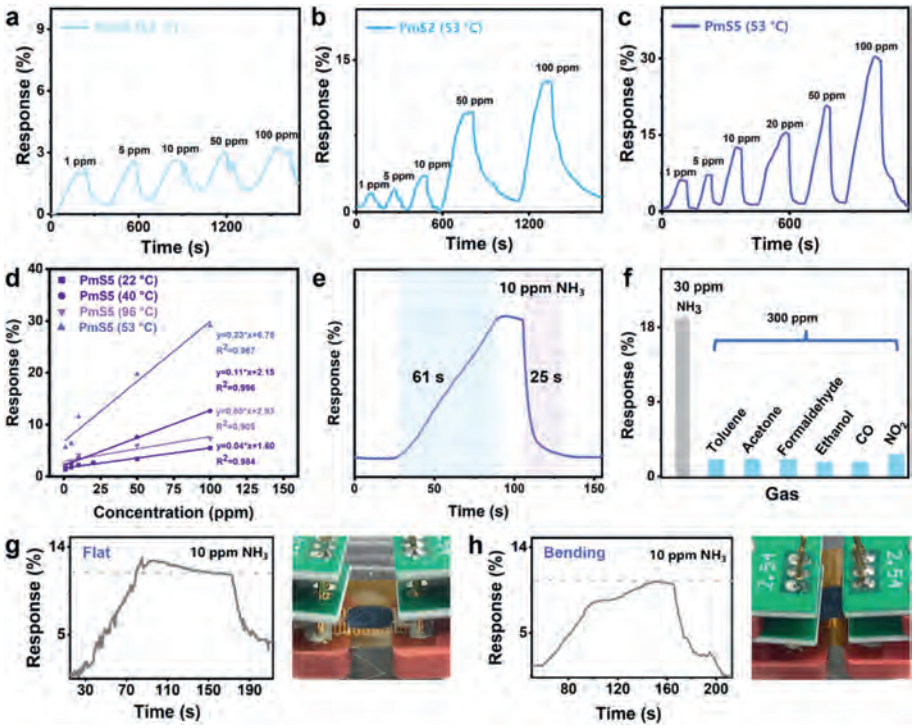


Fig. 4. (a-c) Dynamic response-recovery curves of PmS0, PmS2 and PmS5 based sensor at a heating voltage of 2.5 V (53 °C). (d) Linear fitting curves of the PmS5-based sensors between the response values and NH_3 concentration at different temperature. (e) Response/recovery time of the PmS5-based sensor at a heating voltage of 2.5 V (53 °C) in response to 10 ppm NH_3. (f) Selective responses of the PmS5-based sensors toward various gases. Response-recovery curve of the PmS5-based sensors to 10 ppm NH_3 under (g) straight condition, (h) bending condition.

formation conditions (Fig. 3c). With an applied voltage of 4 V, the heating component shows the temperature of 114.7 and 109.7 °C, under bending and twisting conditions, respectively, which are comparable to the value of 110.3 °C in straight condition. Moreover, 15 cycles of bending tests at voltage of 2.5 also confirmed the excellent stability of the device (Fig. 3d), highlighting its potential for flexible and wearable applications. Furthermore, after producing PmS5 layer on the device, the resistance of the sensitive layer was measured under different bending states at room temperature. The results confirm the sensor's reliable performance and its ability to function consistently in deformed configurations (Fig. 3e). The strong adhesion between the sensing ink and the substrate ensures that the flexible sensor maintains excellent stability even under various bending angles.

Ammonia (NH_3) is an important but harmful compound which is widely used as a raw material in global agriculture and industry [38–40]. Additionally, as a product of metabolism, NH_3 has been recognized as an important biomarker in exhaled breath that can be used in noninvasive diagnosing diseases such as Helicobacter pylori-induced peptic ulcers and kidney disorders [41–43]. Therefore, NH_3 monitoring is critical for ensuring environmental safety and human healthcare [44]. In this study, the application possibility of the obtained flexible gas sensors for in NH_3 detection was studied. The gas sensing performance of the as-fabricated flexible sensors was assessed with lab-made gas resistance measurement system (Fig. S14 in Supporting information). More details about the measurement procedure are available in Supporting information. Upon exposure to the NH_3 atmosphere, the resistance of the sensor increased rapidly. The resistance returned to its original value (*i.e.*, baseline resistance) after the removal of the NH_3 atmosphere *via* exposing the device to clean air. The response (S) was determined as Eq. 1.

$$S = \frac{R_g - R_a}{R_a} \quad (1)$$

The R_a and R_g are the resistances of sensors in ambient air and the target analyte, respectively. Besides, the response and recovery times were defined as the times for the sensor output to reach 90 % of the saturation response value after applying or switching off the target gas in a step function.

The dynamic response-recovery curves of PmS0, PmS2 and PmS5 based sensors toward NH_3, which were recorded by exposing the device to NH_3 vapor with varying concentration (1–100 ppm) at a heating voltage of 2.5 V, corresponding to a working temperature of 53 °C. From Figs. 4a-c, it can be seen that, the PmS0 based sensor exhibited lower response of 1.4 %–5.5 % than that of PmS2 (1.8 %–12.9 %) and PmS5 (6.0 %–30.5 %) sensors toward 1–100 ppm ammonia. Therefore, the presence of mesoporos SnO_2 can significantly enhance the sensing performance of PmSn sensors. However, excessive mesoporous SnO_2 (>5 wt%) can decrease the quality of sensing layer in terms of homogeneity and adhesion stability on PI, which compromises the stability of the sensing layer. The response increases proportionally with the concentration of NH_3, demonstrating its high sensing activity. Taking the PmS5-sensor as an example, the responses were 6.0 %, 8.1 %, 11.8 %, 16.3 %, 21.2 %, and 30.5 % when contacting NH_3 concentrations of 1, 5, 10, 20, 50, and 100 ppm, respectively. It reveals a wide detection range of the flexible sensors, highlighting their potential for practical applications in NH_3 detection.

Linear fitting curves were analyzed to evaluate the relationship between the response values and NH_3 concentration at different temperatures, providing insights into the optimal operating temperature for the sensor (Fig. 4d and Figs. S15-S17 in Supporting information). The results indicated that the sensor achieved its best performance at a heating voltage of 2.5 V, corresponding to a temperature of 53 °C. Although elevating temperature can improve the carrier concentration in the sensitive material and enhance the gas-sensing response, too high temperature can cause the evaporation of NH_3 molecules and reduce their interaction with PmSn

materials, thereby resulting in lower sensing response. Notably, the sensor demonstrated a strong linear relationship between the response and NH_3 concentration, with a high correlation coefficient ($R^2 = 0.967$), confirming its reliability for quantitative analysis. Furthermore, thanks to the highly porous structure of the PmSn sensing layer, the PmS5 based sensor exhibited rapid response and recovery times of 61 s and 25 s (Fig. 4e) when exposed to 10 ppm NH_3. To study the long-term stability, the PmS5-sensor was exposed to 10 ppm NH_3 for seven consecutive days at 53 °C. The response and R_a did not flatulate significantly (<10 % and 1 %), reflecting good long-term stability toward NH_3 (Fig. S18 in Supporting information). To the best of our knowledge, compared with previously reported NH_3 gas sensors (Table S1 in Supporting information), the PmSn-based sensors possess the best comprehensive performance.

The selectivity is a critical parameter for sensors, particularly in practical applications. To evaluate the sensors' sensing selectivity, the sensors were exposed to 50 ppm NH_3, and 300 ppm of intereference gases, including formaldehyde, toluene, ethanol, carbon monoxide (CO) and nitrogen dioxide (NO_2), respectively, in the test chamber. The sensor showed a significantly higher response of 20 % to NH_3 at 50 ppm than that to toluene (1.93 %), acetone (1.98 %), formaldehyde (1.95 %), ethanol (1.60 %), CO (1.63 %) and NO_2 (2.52 %) at 300 ppm (Fig. 4f), demonstrating an excellent selectivity of the sensors in detection in complex gas environments. In order to study the effect of the humidity to sensor performance, the response of PmS5-sensor toward 10 ppm NH_3 was tested under an atmosphere with relative humidity of 32 %, 51 %, 70 %, respectively (Fig. S19 in Supporting information). As the relative humidity increasing, the response also increased from 11.6 % to 14.5 %, which is attribute to the simultaneous presence of H_2O vapor and NH_3, which produces NH_4^+ and OH^- ions, while the moisture also interacts with PSS chains in PEDOT:PSS, generating PSS (SO_3^-) species. The accumulation of these anions markedly raises the sensor's resistance. Additionally, water vapor increases the interchain distance between PEDOT segments, disrupting charge transport pathways and further elevating the initial resistance and sensing response.

In order to evaluate the mechanical flexibility of the sensors, the responses of the PmS5-based sensors exposed to 10 ppm NH_3 were recorded under both flat and bending conditions (Figs. 4g and h). The sensors exhibit fast response to 10 ppm NH_3 with a response of 11.8 % at straight condition, and the response is about 11.2 % when the flexible sensor was in bending state at about 90°, demonstrating its good stability and reliability for practical applications. Besides, the life-span of the sensor in consecutive bending was measured (Fig. S20 in Supporting information). Compared with the initial state, after 10, 20, 30, 40 and 50 bending cycles, the response of PmS5 sensor to 50 ppm NH_3 decreased by 1, 0.6, 0.4 and 0.3 %, respectively, which is within a small certain range. The flexible gas sensor was further integrated into a wearable low-power smart wristband with wirelessly transmitting detection signals to intelligent display terminals *via* Bluetooth (Fig. 5a, Figs. S21 and S22 in Supporting information). This wearable smart wristband offers promising applications in a variety of scenarios, such as health monitoring for disease diagnosis, environmental monitoring, and toxic gas detection in industrial settings. The smart wristband with flexbile ammonia sensors is highly wearable and portable (Figs. 5b and c). To further evaluate its functionality, the wristband was placed in a chamber to test its response to 50 ppm NH_3 gas (Fig. 5d).

It is well known, the sensing mechanism of the PEDOT:PSS-based NH_3 gas sensor involves reversible redox and proton-exchange reactions during the adsorption and desorption of NH_3 molecules by virtue of its positively charged $PEDOT^+$ and negatively charged PSS^-. Upon exposure to ammonia, $PEDOT^+$ is reduced to its neutral form ($PEDOT^0$) and NH_3 is oxidized to NH_3^+.

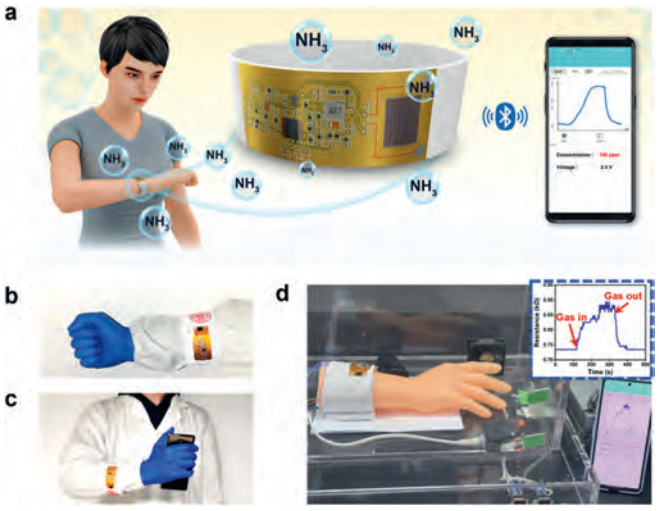


Fig. 5. (a) Schematic diagram of the wearable smart wristband based on PmS5-based sensor. (b) Photograph of the right arm of a volunteer wearing the wearable smart wristband. (c) Photograph the user using the wearable smart wristband to monitor the response towards the gas through mobile phone. (d) Response-recovery curve of the wearable smart wristband to 50 ppm NH_3.

Simultaneously, the -SO_3H group of PSS^- captures NH_3 and form NH_4^+ through proton transfer, leading to an increase in resistance. Upon NH_3 desorption, $PEDOT^0$ is re-oxidized to $PEDOT^+$, and NH_4^+ decomposes into NH_3 and H^+, with H^+ returning to PEDOT:PSS to restore its resistance. This reversible process enables the PEDOT:PSS sensor to respond reliably to NH_3 exposure and removal cycles.

The results about the PmS2, PmS5-based sensor exhibits a significantly higher response compared to the PmS0-based sensor, attributed to the composite sensitization effect which resulted from the formation of p-n heterojunctions at the interface between the inorganic n-type mesoporous SnO_2 and organic p-type PEDOT:PSS (Fig. 6). When PEDOT:PSS contact with the mesoporous SnO_2, the charge carrier concentration gradient between the two materials drives electrons in SnO_2 and holes in PEDOT:PSS to diffuse until a dynamic equilibrium is established, resulting in the forma-

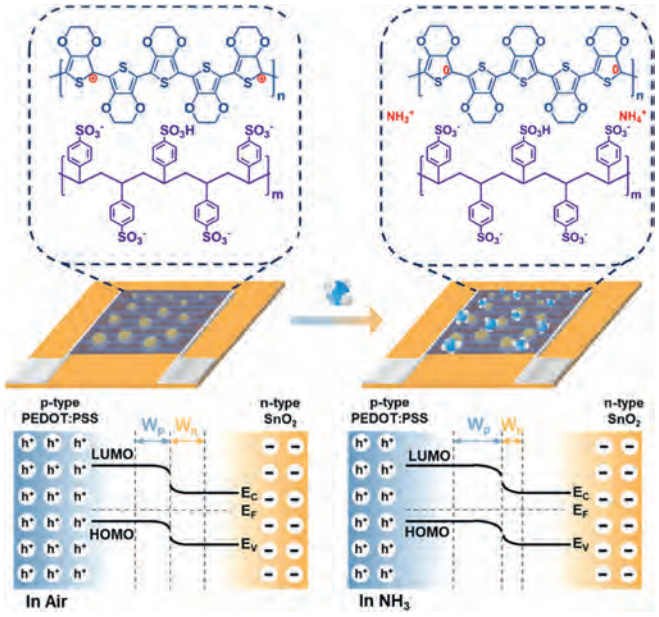


Fig. 6. Sensing mechanism of SnO_2/PEDOT:PSS composite sensing materials to NH_3.

tion of p-n heterojunctions and depletion regions at the interface. These huge heterojunctions increase the resistance of the sensor and decrease the hole concentrations of the p-type semiconductor materials in air, thereby improving sensitivity. In order to confirm this, the initial resistance of different sensing material (PmS0, PmS2, PmS5 and PS5) were tested (Fig. S23 in Supporting information). The resistance of PmS5 is 735 Ω much higher than that of PmS0 (68 Ω), PmS2 (278 Ω) and PS5 (321 Ω), indicating that heterojunction interface can be controlled by adjusting the content of SnO_2 and the mesoporous SnO_2 and rough surface processed by mesopores is benefit for enrichng the heterojunction compared with nonporous strcture. Upon exposure to NH_3, PEDOT:PSS can capture NH_3 molecules to form NH^{4+}/NH^{3+}, which endow the reduce of charge carriers numberand depletion layer thickness, accounting for the significantly enahnced increase of the resistance.

In summary, a new functional colloidal ink consisting of mesoporous SnO_2 and PEDOT:PSS was prepared for direct construction of hierachically porous composite layer on PI substrates combining dispensing printing and freeze-drying strategy. Compared with PEDOT:PSS based sensor, the obtained flexible ammonia sensors have uniform sensing layer stably supported on PI substrate and they exhibited significantly ehanced response, good selectivity to NH_3, fast response and recovery speed (61 s/25 s) and reliable sensing perforamnce against bending and twisting. The enhanced gas sensing performance is mainly due to the rich p-n heterojunction between PEDOT:PSS and hierachially porous structure, facilitating the diffusion of ammonia molecules and their interaction with the composites. The obtained flexible sensors have great potential for developing smart wearable electronics for various applications including healthcare monitoring. The strategy of combination printing and freeze-drying to form hierarchically organic-inorganic hybrid porous sensing layer provides an efficient and economical approach for the large-scale preparation of functional nanomaterials with high specific surface area in fabricating nanodevices. By tailoring the composition of the hybrid ink, it can be extended to develop other hybrid materials for exploring composites with enhanced optical, electronic and thermal properties.

Declaration of competing interest

The authors declare that they have no known competing financial interests or personal relationships that could have appeared to influence the work reported in this paper.

CRediT authorship contribution statement

Yidan Chen: Writing – review & editing, Writing – original draft, Validation, Methodology, Investigation. **Luyang Liu:** Writing – review & editing, Writing – original draft, Investigation. **Jichun Li:** Writing – review & editing, Writing – original draft, Investigation. **Yu Deng:** Writing – review & editing, Writing – original draft, Investigation. **Hongxiu Yu:** Writing – review & editing, Writing – original draft, Resources, Funding acquisition. **Kaiping Yuan:** Writing – review & editing, Writing – original draft, Supervision. **Yuanyuan Zhang:** Writing – review & editing, Investigation. **Yu Wang:** Supervision. **Yonghui Deng:** Writing – review & editing, Writing – original draft, Supervision, Funding acquisition, Conceptualization.

Acknowledgments

This work was financially supported by National Key R&D Program of China (No. 2024YFD2402203), NSF of China (Nos. 22125501, U22A20152), Science and Technology Commission of Shanghai Municipality (No. 2024ZDSYS02), and Fundamental Research Funds for the Central Universities (No. 20720220010).

Supplementary materials

Supplementary material associated with this article can be found, in the online version, at doi:10.1016/j.cclet.2025.111654.

References

[1] C. Oh, H.J. Lee, Nat. Electron. 7 (2024) 1070–1071.
[2] P.G. Steeneken, E. Kaiser, G.J. Verbiest, et al., Nat. Rev. Method. Prim. 3 (2023) 60.
[3] K. Mahato, T. Saha, S. Ding, et al., Nat. Electron. 7 (2024) 735–750.
[4] R.A. Potyrailo, Chem. Rev. 116 (2016) 11877–11923.
[5] Y. Lu, H. Zhang, Y. Zhao, et al., Adv. Mater. 36 (2024) 2310613.
[6] I. Cho, K. Lee, Y.C. Sim, et al., Light Sci. Appl. 12 (2023) 95.
[7] J. Xu, X. Fan, K. Xu, et al., Nano-Micro Lett. 17 (2025) 115.
[8] Y.M. Jo, Y.K. Jo, J.H. Lee, et al., Adv. Mater. 35 (2023) 2206842.
[9] H.J. Han, S.H. Cho, S. Han, et al., Adv. Mater. 33 (2021) 2170350.
[10] J. Ma, Y. Li, J. Li, et al., Adv. Funct. Mater. 32 (2022) 2107439.
[11] B. Feng, Z. Wang, Y. Feng, et al., ACS Nano 18 (2024) 22888–22900.
[12] S. Park, M. Kim, Y. Lim, et al., Adv. Mater. 36 (2024) 2313731.
[13] Z. Wu, H. Wang, Q. Ding, et al., Adv. Funct. Mater. 33 (2023) 2300046.
[14] Y. Men, Z. Qin, Z. Yang, et al., Adv. Funct. Mater. 34 (2024) 2316633.
[15] Y. Zhou, Y. Zhang, Y. Zhou, et al., Nano Energy 117 (2023) 108881.
[16] S. Kim, J. Han, J.M. Choi, et al., Adv. Mater. 36 (2024) 2313830.
[17] J. Lee, J.H. Chun, Y. Kim, et al., ACS Nano 19 (2025) 5515–5525.
[18] L.X. Ou, M.Y. Liu, L.Y. Zhu, et al., Nano-Micro Lett. 14 (2022) 206.
[19] W. Xing, J. Wang, Q. Qian, et al., ACS Appl. Mater. Interfaces 15 (2023) 57717–57725.
[20] D. Ludescher, P. Ruchka, L. Siegle, et al., Adv. Opt. Mater. 13 (2025) 2403271.
[21] X. Liu, W. Zheng, R. Kumar, et al., Coord. Chem. Rev. 462 (2022) 214517.
[22] C. Zhu, X. Dong, C. Guo, et al., J. Mater. Chem. A 10 (2022) 12150–12156.
[23] S.Mohseni Taromsari, M. Salari, H.H. Shi, et al., Adv. Mater. 37 (2025) 2406349.
[24] S.H. Lee, J. Han, O.S. Jeon, et al., Compos. Pt. B. 275 (2024) 111305.
[25] D. Lv, W. Chen, W. Shen, et al., Sensor Actuat. B: Chem. 298 (2019) 126890.
[26] L. Jin, K. Yang, L. Chen, et al., Anal. Chem. 95 (2023) 8859–8868.
[27] X. Tian, S. Wang, B. Yao, et al., J. Hazard. Mater. 465 (2024) 133195.
[28] Y. Lin, L. Huang, L. Chen, et al., Sensor Actuat. B: Chem. 216 (2015) 176–183.
[29] E. Zampetti, S. Pantalei, A. Muzyczuk, et al., Sensor Actuat. B: Chem. 176 (2013) 390–398.
[30] Y. Li, Y. Zhang, Y. Zhou, et al., ACS Sens. 8 (2023) 4132–4142.
[31] T.Ramos Canabarra Dos Santos, M. De Jesus Bassi, M. Muller De França, et al., ACS Appl. Mater. Interfaces 17 (2025) 13065–13073.
[32] O. Ogbeide, G. Bae, W. Yu, et al., Adv. Funct. Mater. 32 (2022) 2113348.
[33] J. Shin, K. Kim, I.S. Min, et al., Adv. Funct. Mater. 35 (2025) 2419110.
[34] P. Manjula, R. Boppella, S.V. Manorama, ACS Appl. Mater. Interfaces 4 (2012) 6252–6260.
[35] L.V. Kayser, D.J. Lipomi, Adv. Mater. 31 (2019) 1806133.
[36] H. Zhu, Q. Li, C. Yang, et al., J. Am. Chem. Soc. 140 (2018) 7403–7406.
[37] D. Ni, Y. Chen, H. Song, et al., J. Mater. Chem. A 7 (2019) 1323–1333.
[38] X. Fu, J.B. Pedersen, Y. Zhou, et al., Science 379 (2023) 707–712.
[39] S. Li, Y. Zhou, K. Li, et al., Joule 6 (2022) 2083–2101.
[40] J. Li, L. He, X. Liu, et al., Angew. Chem. Int. Ed. 58 (2019) 1759–1763.
[41] H. Chen, Y. Chen, H. Zhang, et al., Adv. Funct. Mater. 28 (2018) 1801035.
[42] P. Gong, S. Yuan, Z. Yu, et al., J. Am. Chem. Soc 146 (2024) 4036–4044.
[43] G. Song, D. Jiang, J. Wu, et al., Chem. Eng. J. 440 (2022) 135979.
[44] D.H. Kim, J.H. Cha, J.Y. Lim, et al., ACS Nano 14 (2020) 16907–16918.